

# Relative-humidity profiling in the troposphere with a Raman lidar

Ina Mattis, Albert Ansmann, Dietrich Althausen, Volker Jaenisch, Ulla Wandinger, Detlef Müller, Yuri F. Arshinov, Sergej M. Bobrovnikov, and Ilya B. Serikov

We describe a Raman-lidar-based approach to acquiring profiles of the relative humidity of air. For this purpose we combined in one instrument the Raman-lidar techniques that are used for the profiling of water vapor and temperature. This approach enabled us to acquire, for the first time to our knowledge, vertical profiles of relative humidity through the entire troposphere exclusively from Raman-lidar data. The methods applied to determining the water-vapor mixing ratio, temperature, and relative humidity and the corresponding uncertainties caused by systematic errors and signal noise are presented. The lidar-derived profiles are compared with profiles measured with radiosondes. Radiosonde observations are also used to calibrate the Raman lidar. Close agreement of the profiles of relative humidity measured with lidar and those measured with radiosonde demonstrates the potential of this novel approach.

© 2002 Optical Society of America

OCIS codes: 010.3640, 010.7030, 280.0280, 290.5860.

## 1. Introduction

Relative humidity is one of the most important parameters in the description of the physical state of the atmosphere. It controls cloud formation and aerosol optical properties and thus visibility. Condensation of water vapor is a significant source of sensible heat. Global radiosonde observations provide most of the relative-humidity information required as input in weather-forecast models. However, it is well known that radiosonde measurements are often not reliable at upper-tropospheric temperatures (see Refs. 1–3 concerning Vaisala RS80-A radiosondes). Furthermore, the temporal resolution of routine observations performed by weather services is rather low, with typically two radiosonde launches per day. Therefore important weather phenomena such as the development of the convective boundary layer and the passage of cold and warm fronts cannot be resolved.

Radiosondes take only one data point per measurement height. Thus the measured relative-humidity profiles are often not representative.

For these reasons, alternatives to routine radiosonde observations are required. In addition to remote sensing from space, a reasonable alternative could be a combined lidar–radiosonde network. Lidar measurements are possible whenever the laser beam is not blocked by clouds. The combination of the traditional radiosonde observation with state-of-the-art lidar significantly improves measured tropospheric humidity data sets. It is expected that a temperature–humidity Raman lidar will provide relative-humidity profiles with a relative error of 10%, a vertical resolution from 100 m (boundary layer) to 500–1000 m (free troposphere), and a temporal resolution from 10 min (boundary layer) to 60 min (free troposphere) up to 5–7-km height at daytime and throughout the troposphere during nighttime. Such observations will be much better at meeting the requirements of present and next-generation regional and global atmospheric models and the needs of atmospheric research.<sup>4</sup> Numerical weather prediction has become increasingly more focused on regional and local weather (so-called nowcasting, and short-term forecasting). Meteorological data in the form of 10–60-minute mean profiles are most useful for model initialization and data assimilation. Boundary-layer research needs profiling of atmospheric state parameters with a resolution of 20–150

---

I. Mattis, A. Ansmann (albert.ansmann@tropos.de), D. Althausen, V. Jaenisch, U. Wandinger, and D. Müller are with the Institute for Tropospheric Research, Permoserstrasse 15, 04318 Leipzig, Germany. Y. F. Arshinov, S. M. Bobrovnikov, and I. B. Serikov are with the Institute for Atmospheric Optics, Siberian Branch of the Russian Academy of Sciences, 1, Akademicheskii Avenue, 643055 Tomsk, Russia.

Received 12 February 2002; revised manuscript received 5 July 2002.

0003-6935/02/306451-12\$15.00/0

© 2002 Optical Society of America

m in space and 1–15 min in time to characterize vertical fluxes of moisture, temperature, and pollution properly. Vertical profiling of relative humidity with high spatial and temporal resolution may also allow one to study in detail, e.g., cloud formation processes at the top of the boundary layer. Furthermore, Raman lidars are powerful tools for aerosol monitoring.<sup>5–15</sup> Aerosol and relative-humidity observations with one lidar and thus in the same air volume are an attractive approach to studying aerosol–climate interactions, because the optical properties of particles depend strongly on relative humidity.<sup>9,16</sup>

Although techniques for accurate observation of absolute humidity and of water-vapor-to-dry-air mixing ratios with differential absorption lidar and Raman lidar, respectively, are available (the latest developments may be found in Refs. 15 and 17–25), the potential of lidar to measure tropospheric relative-humidity profiles has not been demonstrated. The main reason is that determining relative humidity requires simultaneous observation of temperature and water vapor. However, the lidar measurement of temperature has not yet become a routine practice. The temperature differential absorption lidar technique<sup>26</sup> failed to permit trustworthy temperature profiling.<sup>27</sup> The Rayleigh-to-aerosol backscatter ratio must be known rather accurately in this approach if one is to determine the temperature with 1–2-K uncertainty. However, under typical boundary-layer aerosol conditions and for realistic uncertainties in the lidar-derived backscatter ratio the temperature error is of the order of 5 K. Accurate temperature measurements with differential absorption lidar are possible only in rather hazy (negligible molecular backscattering) or rather clean conditions in the upper free troposphere (negligible particle backscattering). In contrast, the rotational Raman-lidar technology<sup>28–34</sup> now allows one to measure temperature profiles through the troposphere, as is shown below.

An alternative to temperature measurements with lidar is profiling by means of the radio acoustic sounding system (RASS).<sup>35</sup> Less than 0.3-K bias and 0.4–0.7-K standard deviation of temperature differences between the RASS (10-min averages) and radio sounding can be achieved. However, standard RASS permits routine temperature profiling only up to heights of 5–6 km.<sup>36</sup>

Another alternative to use of lidar is the retrieval of the vertical temperature profile with the Atmospheric Emitted Radiance Interferometer (AERI).<sup>37</sup> At the Southern Great Plains Cloud and Radiation Testbed site of the Atmospheric Radiation Measurement program it was demonstrated that a combination of an automated Raman lidar for the profiling of the water-vapor mixing ratio and an automated AERI for the retrieval of the temperature profiles can give detailed information on the diurnal cycle of moisture, temperature, and relative humidity in the lower troposphere with 10-min resolution.<sup>38</sup> Sharp and strong inversion layers, however, are hard to retrieve from the measured radiances.<sup>37</sup> As a consequence,

the uncertainty in the relative humidity is large in these inversion layers. In addition, clouds may affect the retrievals.

In this paper we present, to our knowledge for the first time, relative-humidity observations from the ground to the tropopause that are based exclusively on lidar. Radiosondes (Vaisala RS80-A) are used to calibrate the lidar system. In fact, Raman-lidar techniques for water-vapor and temperature profiling theoretically do not need calibration with radiosondes. The latter are used following a tradition to compare measurement data obtained independently. Compared with Rayleigh and aerosol backscatter signals, Raman signals are weak. Raman lidars work best under nighttime conditions, i.e., in the absence of sky background light. However, recently it was demonstrated that temperature profiling up to stratospheric heights at daytime is feasible.<sup>39–41</sup> Successful daytime water-vapor measurements up to the middle free troposphere have also been reported.<sup>19,42</sup> Whereas the measurements presented here are limited to nighttime periods, the previous measurements point toward the possibility of daytime relative-humidity measurements with Raman lidar.

In Section 2 the main features of our Raman lidar are outlined. After summarizing the well-established Raman lidar methods for the determination of tropospheric water-vapor-to-dry-air mixing ratio and air temperature, we present a method for computation of the relative humidity (Section 3). Experiments are discussed in Section 4, together with an extended error analysis. Concluding remarks are given in Section 5.

## 2. Instrumentation

In recent years, the lidar group of the Institute for Tropospheric Research has been engaged in routine lidar observations of the troposphere within the framework of the German aerosol lidar network<sup>43–45</sup> and the European Aerosol Research Lidar Network.<sup>46</sup> In these projects, profiles of atmospheric water-vapor mixing ratios and temperatures are acquired, together with profiles of particle optical parameters of the atmosphere. The observations are performed with a combined Raman elastic-backscatter lidar. The combination of water-vapor-mixing-ratio and temperature profiles enables us to derive profiles of the relative humidity of air.

A block diagram of the lidar is presented in Fig. 1. The source of radiation is a Spectra-Physics GCR-290-30 Nd:YAG laser. It delivers pulses at three wavelengths (1064, 532, and 354 nm) simultaneously, with a total pulse energy of as much as 1.6 J. Laser shots are fired at a repetition rate of 30 Hz. The outgoing beam is collimated with a beam expander that has a magnification factor of 10 before it is directed to the atmosphere by a beam-folding mirror. A 1-m-diameter Cassegrainian telescope collects radiation that has been backscattered by atmospheric molecules and particles.

We employ the elastic backscattering at the three emitted wavelengths, including information on the

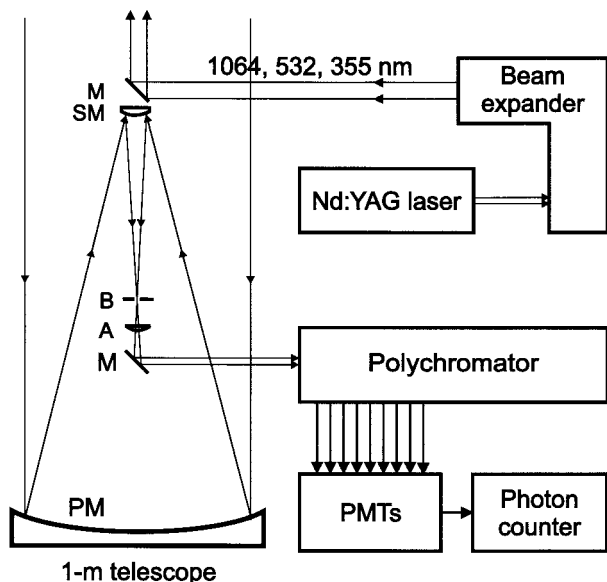


Fig. 1. Schematic view of the Raman lidar. Three laser beams, at 355, 532, and 1064 nm, are transmitted vertically into the atmosphere by way of a mirror (M). The Cassegrain telescope consists of a primary mirror (PM), a secondary mirror (SM), a field stop (B), an achromatic lens (A), and a mirror to direct the back-scattered photons to the beam-separation unit. PMT, photomultiplier tube.

depolarization at 532 nm, to study the height stratification and some optical and microstructure properties of the atmospheric aerosol. In addition, we record Raman-lidar returns from the main molecular constituents of the atmosphere, namely, nitrogen and water vapor, to acquire profiles of temperature and moisture content as well as particle extinction coefficients of the atmosphere. To obtain the water-vapor profile<sup>47</sup> we use radiation at 355 nm to excite lidar returns from the  $\nu_1$  vibrational-rotational Raman band of water vapor centered at 407 nm and from nitrogen at 387 nm. To obtain the temperature profile we isolate four portions from the Stokes and anti-Stokes branches of the pure rotational Raman spectrum (PRRS) of nitrogen excited by radiation of the second harmonic of the Nd:YAG laser. The technique is described in Ref. 48. The discrimination of the PRRS of nitrogen against the sky background is done with a Fabry-Perot interferometer (FPI) according to the technique described in Ref. 49. The transmission comb of the FPI is tuned to transmit the comb of the nitrogen PRRS and simultaneously to reject the comb of the oxygen PRRS, as the latter has a period different from that of nitrogen. We use the  $\nu_1$  vibrational-rotational Raman bands of nitrogen at 387 and 607 nm—the latter excited by radiation at 532 nm—to determine particle extinction profiles after the method described in Ref. 5.

All in all, we have to isolate optically 12 lidar returns: three returns that are due to unshifted scattering at wavelengths of 1064, 532, and 355 nm without discrimination between the polarization components; four returns within the Stokes and anti-

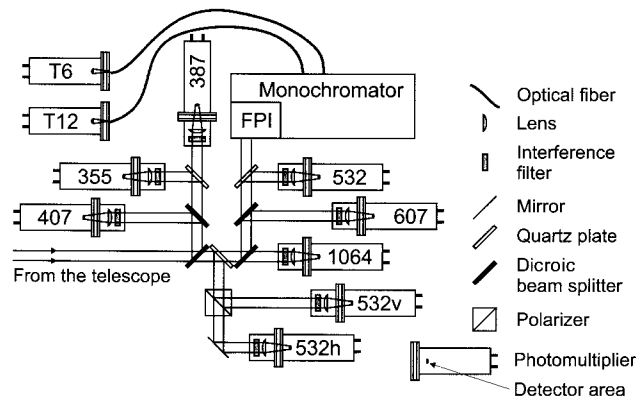


Fig. 2. Schematic view of the beam-separation unit. The numbers indicate the measurement wavelengths in nanometers. T6 and T12, detectors for the pure rotational Raman signals. 532v and 532h, cross-polarized and parallel-polarized 532-nm signal components, respectively, with respect to the transmitted laser light.

Stokes portions of the PRRS of nitrogen excited by radiation at 532 nm; two returns within the vibrational-rotational Raman band of nitrogen at 387 and 607 nm excited by radiation at 355 and 532 nm, respectively; the Raman-lidar return from water vapor at 407 nm excited by radiation at 355 nm; and two returns from the parallel-polarized and cross-polarized components of the unshifted scattering at 532 nm. We use a combination of different spectroscopic devices to spectrally isolate the lidar returns. The optical arrangement of the polychromator is presented in Fig. 2. The elastic signals and the vibrational-rotational Raman bands of nitrogen and water vapor are isolated with dichroic mirrors and interference filters. The major portion of the back-scattered radiation at 532 nm, including the Stokes and the anti-Stokes branches of the PRRS of nitrogen, passes dichroic mirrors and a couple of quartz-plate beam splitters and the FPI, and is then directed to a monofiber-coupled double-grating monochromator that isolates four portions from the Stokes and anti-Stokes branches. At the exit of the double-grating monochromator two optical signals are formed from these four portions.<sup>48</sup> The intensity ratio bears information on temperature. The retrieval of the temperature profile from this intensity ratio is described in Ref. 30. All optical signals of the lidar are recorded with Thorn EMI photomultiplier tubes (PMTs) in the photon-counting mode.

It is worth noting the ability of the spectroscopic units to suppress stray light from unshifted (particle + molecular) scattering in the water-vapor and temperature channels. This property provides for a high spectral purity of the Raman-lidar returns, which is critical for the quality of any Raman-lidar data. The combination of interference filters and dichroic mirrors that is used to isolate the return signal of the vibrational-rotational Raman band of nitrogen at 387 nm provides a rejection of this stray light by a factor of at least  $10^8$ . The level of stray-light rejection at 407 nm, i.e., at the water-vapor vibrational-

rotational Raman band, is  $\sim 10^{10}$ . The combination of the FPI and the double-grating spectrometer has a rejection of at least  $10^9$  with respect to the unshifted scattering of radiation at 532-nm wavelength.

Finally, referring to the argument that only the anti-Stokes parts of the spectrum should be used in the determination of temperature,<sup>32,34</sup> we mention that we have never noticed any influence of fluorescence. At least, aerosol fluorescence seems to play no role here. Even when aerosol conditions vary strongly with height, we have never found indications of any correlation between the derived temperatures and backscatter coefficients except in those cases that can be explained by meteorological conditions (e.g., the coincidence of backscatter peaks at the tops of inversion layers).

### 3. Method

On the basis of the combination of the Raman-lidar technologies developed for temperature<sup>28–34,41,50</sup> and moisture<sup>8,19,21,22,24,38,42,47,51–63</sup> profiling, it is possible to determine profiles of relative humidity. For this purpose temperature profiles and profiles of the water-vapor mixing ratio are measured simultaneously with the pure-rotational Raman-lidar channel and the water-vapor Raman-lidar channel. The methodological basis for retrieving profiles of relative humidity from Raman-lidar data is described by a set of lidar equations. Normally, Raman-lidar returns are recorded in the so-called photon-counting mode. In this case the intensity of the  $i$ th Raman-lidar return of a multichannel system is represented by the number of photocounts:

$$P_i(z) = \frac{K_i O_i(z)}{z^2} \beta_i(z) \Delta z \times \exp \left[ - \int_0^z [\alpha_{\lambda_0}(\zeta) + \alpha_{\lambda_i}(\zeta)] d\zeta \right]. \quad (1)$$

The range gate is described by  $\Delta z$ ; the sounding range is  $z$ .  $K_i$  is the system constant for channel  $i$ . It comprises all system parameters, such as the efficiency of the optical channels and the quantum efficiency of the photodetectors.  $O_i(z)$  is the geometrical factor, or the overlap function, that describes the overlap between the laser beam and the receiver's field of view.  $\beta_i(z)$  denotes the backscattering coefficient of a molecular species as a function of range.  $\alpha_{\lambda_0}(z)$  and  $\alpha_{\lambda_i}(z)$  are the profiles of the extinction coefficients of the atmosphere at the wavelengths of the transmitted radiation and of the Raman-shifted lidar return, respectively.

The coefficients of the backscattering from water-vapor and nitrogen molecules are

$$\beta_{\text{H}_2\text{O}}(z) = N_{\text{H}_2\text{O}}(z) \frac{d\sigma_{\text{H}_2\text{O}}(\pi)}{d\Omega}, \quad (2)$$

$$\beta_{\text{N}_2}(z) = N_{\text{N}_2}(z) \frac{d\sigma_{\text{N}_2}(\pi)}{d\Omega}, \quad (3)$$

where  $N_{\text{H}_2\text{O}}(z)$  and  $N_{\text{N}_2}(z)$  are the profiles of water-vapor and nitrogen number densities, respectively, and  $d\sigma_{\text{H}_2\text{O}}(\pi)/d\Omega$  and  $d\sigma_{\text{N}_2}(\pi)/d\Omega$  are the differential cross sections of the Raman backscattering within the rotational–vibrational Raman bands of water-vapor and nitrogen molecules, respectively. The coefficients of pure rotational Raman backscattering from nitrogen molecules (PRRS portions isolated for temperature measurements near the lines, which correspond to transitions from the rotational levels with the rotational quantum numbers  $J_1 = 6$  and  $J_2 = 12$ ) are functions of the temperature profile  $T(z)$  along the laser beam,

$$\beta_{J_1}(z) = F_1[T(z)], \quad (4)$$

$$\beta_{J_2}(z) = F_2[T(z)], \quad (5)$$

because of the Boltzmann distribution of the molecular population over the rotational energy states. The explicit form of the temperature dependence of the intensities of the PRRS lines can be found elsewhere.<sup>28,30,32</sup>

#### A. Water-Vapor-to-Dry-Air Mixing Ratio

The water-vapor-to-dry-air mixing ratio  $m_{\text{H}_2\text{O}}(z)$  is calculated from the ratio of the lidar returns from water-vapor and nitrogen molecules. From Eqs. (1)–(3) follows

$$m_{\text{H}_2\text{O}}(z) = C^{\text{H}_2\text{O}} \frac{P_{\text{H}_2\text{O}}(z)}{P_{\text{N}_2}(z)} \frac{\exp \left[ - \int_0^z \alpha_{\lambda_{\text{N}_2}}(\zeta) d\zeta \right]}{\exp \left[ - \int_0^z \alpha_{\lambda_{\text{H}_2\text{O}}}(\zeta) d\zeta \right]}, \quad (6)$$

where  $C^{\text{H}_2\text{O}}$  is the lidar calibration coefficient that depends on the instrumental transmission and detection efficiencies at the wavelengths of the Raman returns, on the Raman scattering cross sections after Eqs. (2) and (3), and on the ratio of nitrogen molecule number density and dry-air molecule number density (0.78). The calibration coefficient must be determined for each specific lidar. In principle, the lidar calibration coefficient can be determined by independent methods.<sup>22,58,60</sup> In practice, it is determined by comparison (regression) with simultaneous measurements from a reference instrument: a collocated radiosonde<sup>63</sup> or a microwave radiometer.<sup>42</sup> In Ref. 22 an excellent overview of available calibration methods is provided.

In Eq. (6) the overlap functions  $O_{\text{H}_2\text{O}}(z)$  and  $O_{\text{N}_2}(z)$  of the water-vapor and nitrogen Raman-lidar channels are assumed to be identical. The difference between the atmospheric transmissions at  $\lambda_{\text{H}_2\text{O}} = 407$  nm and  $\lambda_{\text{N}_2} = 387$  nm is caused mainly by Rayleigh scattering and can easily be corrected for by use of standard-atmospheric profiles of temperature and pressure or, if available, actual radiosonde data. The meteorological data yield the molecular number density. The Rayleigh scattering cross sections are range independent and are known from the litera-

ture.<sup>64</sup> Differences in transmission at the two Raman wavelengths as a result of wavelength-dependent particle extinction are negligible (<3%) for clear-air conditions. In this case the particle optical depth is  $\leq 0.5$  and the wavelength dependence of particle extinction typically is  $\lambda^{-1}$ .<sup>47,62</sup> The transmission ratio in Eq. (6) may be  $< 0.9$  under very hazy conditions with particle optical depths of  $> 2$  and must be corrected for in these cases.<sup>8,47,60,62</sup> With the system presented here, particle extinction is measured at 355 and 532 nm so the wavelength dependence can be estimated. However, the observations presented in Subsection 3.B were performed at particle optical depths of  $< 0.3$ , so differential transmission effects can be neglected.

The measurement error in the water-vapor mixing ratio,

$$\Delta m_{\text{H}_2\text{O}} = [(\Delta m_{C^{\text{H}_2\text{O}}})^2 + (\Delta m_{\text{stat}})^2]^{1/2}, \quad (7)$$

is estimated according to the laws of error propagation applied to Eq. (6). The systematic error  $\Delta m_{C^{\text{H}_2\text{O}}} = \partial m_{\text{H}_2\text{O}} / \partial C^{\text{H}_2\text{O}} \times \Delta C^{\text{H}_2\text{O}}$  accounts for the uncertainty of the calibration constant  $\Delta C^{\text{H}_2\text{O}}$ . The statistical error  $(\Delta m_{\text{stat}})^2$  comprises terms such as signal noise,  $(\partial m_{\text{H}_2\text{O}} / \partial P_i \times \Delta P_i)^2$  with  $i = \text{H}_2\text{O}, \text{N}_2$ , and further terms that account for error contributions by the background signals (sky background, dark photocounts of the PMTs). The PMT's output signal is assumed to obey Poisson statistics, in which case the variance of the signal equals its mean value; i.e., we can write  $(\Delta P_i)^2 = P_i$ .

#### B. Temperature

The temperature dependence of the signal ratio  $P_{J_1}(z)/P_{J_2}(z)$  is well approximated within an accuracy of 1 K by<sup>30</sup>

$$R[T(z)] = \frac{P_{J_1}(z)}{P_{J_2}(z)} = \frac{\beta_{J_1}(z)}{\beta_{J_2}(z)} \approx \exp\left[\frac{A_T}{T(z)} + B_T\right], \quad (8)$$

where  $A_T$  and  $B_T$  are the calibration constants that are determined by comparison of the temperature profiles acquired with the lidar and a radiosonde. The approximation yields the following simple formula for the temperature profile,  $T(z)$ , calculated from the ratio of the two temperature-dependent pure-rotational Raman-lidar returns:

$$T(z) \cong \frac{A_T}{\ln[R(z)] - B_T}. \quad (9)$$

In a way similar to that for the mixing ratio, one can derive the expression for estimating the uncertainty  $\Delta T$  in the temperature profile:

$$\Delta T = [(\Delta T_{A_T, B_T})^2 + (\Delta T_{\text{stat}})^2]^{1/2}. \quad (10)$$

Again, as in the case of the water-vapor mixing ratio, the uncertainty in the temperature profile is determined by statistics (the number of photocounts) of the lidar returns recorded ( $\Delta T_{\text{stat}}$ ) and by the accuracy of calibration ( $\Delta T_{A_T, B_T}$ ).

#### C. Relative Humidity

Relative humidity (over water) is defined as

$$U_w(z) = \frac{e(z)}{e_w(z)}. \quad (11)$$

The water-vapor pressure is  $e(z)$ , and the saturation pressure is  $e_w(z)$ . The water-vapor pressure is related to the mixing ratio as follows<sup>65</sup>:

$$e(z) = \frac{p(z)m_{\text{H}_2\text{O}}(z)}{0.622 + m_{\text{H}_2\text{O}}(z)}. \quad (12)$$

$p(z)$  is the air pressure and must be estimated from profiles of routine radiosonde measurements or by assuming standard atmospheric conditions. The uncertainty in this estimation is always smaller than 1% and thus is ignored in the error analysis. The saturation vapor pressure depends on temperature according to<sup>66</sup>

$$e_w(z) = 6.107 \exp\left\{\frac{M_A [T(z) - 273]}{M_B + [T(z) - 273]}\right\}, \quad (13)$$

with the constants  $M_A = 17.84, 17.08$  and  $M_B = 245.4, 234.2$  for  $T$  below and above 273 K, respectively. The constants are taken from the 6th edition of the *Smithsonian Meteorological Tables*.<sup>66</sup>

The uncertainty in the relative humidity can be calculated from the errors of saturation pressure  $\Delta e_w$  and the error of water-vapor pressure  $\Delta e$  according to

$$\Delta U_w = \left[ \left( \frac{\partial U_w}{\partial e} \Delta e \right)^2 + \left( \frac{\partial U_w}{\partial e_w} \Delta e_w \right)^2 \right]^{1/2}, \quad (14)$$

$$\Delta e_w = \left[ \left( \frac{\partial e_w}{\partial T} \Delta T \right)^2 \right]^{1/2}, \quad (15)$$

$$\Delta e = \left[ \left( \frac{\partial e}{\partial m_{\text{H}_2\text{O}}} \Delta m_{\text{H}_2\text{O}} \right)^2 \right]^{1/2}. \quad (16)$$

#### 4. Experiment

The Raman lidar must be calibrated before it is used for retrieval of the meteorological parameters. The constants  $C^{\text{H}_2\text{O}}, A_T$ , and  $B_T$  are determined from the radiosonde–lidar comparisons. Figure 3 illustrates the determination of the constant  $C^{\text{H}_2\text{O}}$ . Figure 3a presents the ratio of the water-vapor-mixing-ratio profile acquired with a radiosonde to that calculated from the ratio of the water vapor to the nitrogen lidar return by Eq. (6) with  $C^{\text{H}_2\text{O}} = 1$ . Only radiosonde data for temperatures of  $> -40$  °C have been used in the calibration. Vaisala RS80 values for the relative humidity measured at temperatures of  $< -40$  °C are not reliable.<sup>3,22</sup> The height variations of the calibration constant  $C^{\text{H}_2\text{O}}$  are most likely due to temporal changes in the vertical distribution of moisture during the measurements. The radiosonde was launched at 2010 UTC and reached the height of 7 km in 37 min, whereas the lidar profile is an average over the time period from 1930 to 2132 UTC. Still, we have used the entire profile presented in this fig-

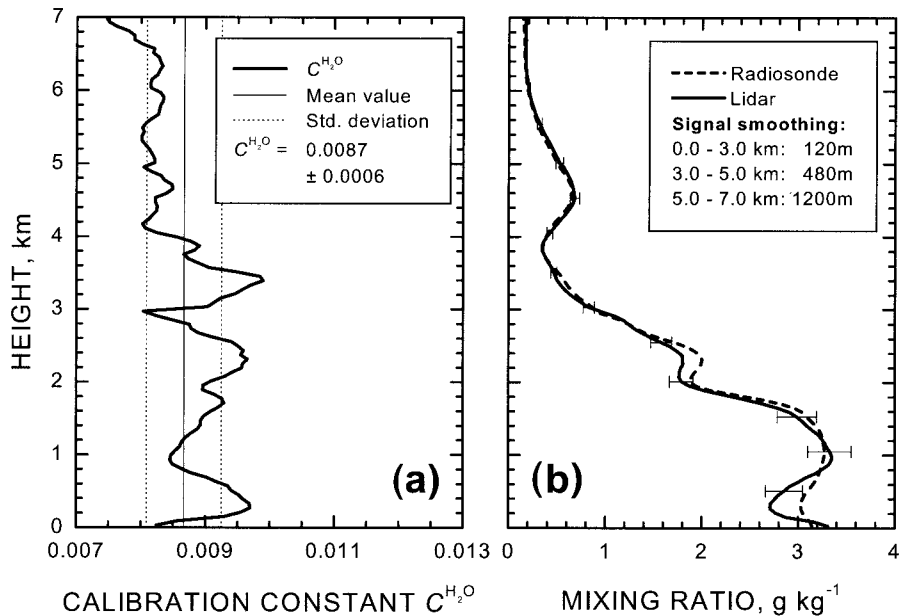


Fig. 3. (a) Calibration constant  $C^{\text{H}_2\text{O}}$  defined as the ratio of the water-vapor mixing ratio measured with the radiosonde and that obtained with an uncalibrated lidar [ $C^{\text{H}_2\text{O}} = 1$  in Eq. (6)]. (b), Mixing ratio measured with radiosonde and determined with a calibrated Raman lidar ( $C^{\text{H}_2\text{O}} = 0.0087$ ). The lidar signals were smoothed before calculation of the mixing ratio to reduce signal noise. The same smoothing lengths were applied to the radiosonde data. Error bars indicate the standard deviation as a function of  $\Delta C^{\text{H}_2\text{O}} (=0.0006)$  and signal noise [cf. Eq. (7)].

ure to calculate the mean value of lidar calibration coefficient  $C^{\text{H}_2\text{O}}$  and to estimate the standard deviation  $\Delta C^{\text{H}_2\text{O}}$  of the calibration coefficient needed in Eq. (7). The profile of the water-vapor-to-dry-air mixing ratio presented in Fig. 3b has been calculated on the basis of the mean value of the constant. The deviation of the mean value of the calibration constant from the profile values (mainly negative below 4 km and positive at all heights above 4 km) is reflected in the difference between the lidar and radiosonde values in Fig. 3b.

The relative error in the calibration coefficient of  $\sim 7\%$  is comparably large. Approximately 15 lidar–radiosonde comparisons were made in 1999–2000. These intercomparisons included cross checks in cases with water clouds in which we assumed a relative humidity of 100% at the cloud base and temperature profiles measured with nearby radiosondes of the German weather service. The variations in the calibration coefficient were found to be close to 5%. It should, however, be mentioned that radiosondes themselves must be calibrated before the launch. Sonde-to-sonde variability in this calibration as well as long-term and short-term drifts in the lidar transmission and detection efficiencies limit precision in the determination of the lidar calibration coefficient. Therefore a calibration method was developed that uses a microwave radiometer as a reference.<sup>42</sup> In this method one compares the total column water-vapor contents measured by the two instruments to deduce the calibration coefficient. A calibration precision of 2–3% was achieved in this way.<sup>42</sup> However, as was pointed out previously,<sup>22</sup> in this procedure the lidar system must be designed to

ensure measurements from the surface throughout the troposphere, which is technically demanding. Furthermore, calibration depends critically on accurate correction for instrumental field-of-view effects, photomultiplier nonlinearity, and the quality of the microwave–radiometer calibration.

Before presenting the experimental results of  $A_T$  and  $B_T$  we need to discuss another effect. Comparisons of temperature profiles acquired with radiosondes and those retrieved from pure-rotational Raman-lidar data revealed a systematic overestimation of temperature determined from lidar data in the height range from  $\sim 0.5$  to  $\sim 2$  km. This effect can be seen in Fig. 4a, where dashed curves show the temperature profiles measured with radiosondes and solid curves show the profiles acquired with the Raman-lidar temperature channel. Figure 4b depicts the ratios of the temperature profiles obtained from the lidar and the radiosonde observations for three different cases. Analysis of the optical arrangement of the lidar temperature-channel arrangement performed later showed that the reason for this artifact is most likely a noticeable sphericity of the FPI plates.<sup>67</sup> We did not observe any significant deviation between the radiosonde- and lidar-derived temperatures in the near zone before integration of the FPI into the system.<sup>33</sup> The influence of this effect can and will be avoided in our new study. Here we corrected for this near-zone bias by means of a distortion function  $F(z)$  (see Fig. 4) that was determined from three independent lidar–radiosonde temperature observations.  $F(z)$  is the ratio of the lidar-derived temperature to the radiosonde temperature. The radiosonde observation is assumed to describe accu-

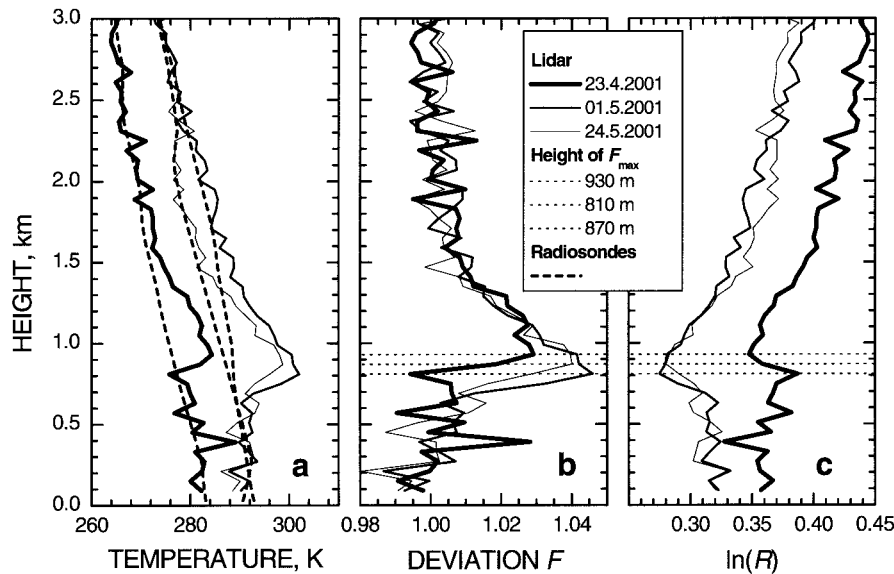


Fig. 4. a, Radiosonde temperature profiles (dashed curves) measured on three days compared with the profiles of  $T(z)$  after Eq. (9). b, Ratio of the lidar-derived temperature to the radiosonde temperature [ $F(z)$ , after Eq. (17)]. c, Logarithm of the ratio of the rotational Raman signals  $\ln(R)$  [see Eq. (8)]. Horizontal lines indicate the maxima of  $F$  and the corresponding minima of  $\ln(R)$ .

rately the vertical temperature distribution during the lidar observation. The true temperature profile is then obtained by

$$T(z) = \frac{T_{\text{lid}}(z)}{F(z)}, \quad (17)$$

where  $T_{\text{lid}}$  is the lidar-derived temperature according to relation (9). The expression for estimating the uncertainty in the temperature measurement now reads [see Eq. (10)] as

$$\Delta T = [(\Delta T_F)^2 + (\Delta T_{A_T, B_T})^2 + (\Delta T_{\text{stat}})^2]^{1/2}. \quad (18)$$

After each test measurement we realigned the temperature channels and the overlap of the laser beam with the field of view of the receiver for reasons of optimization. As a consequence, the height position of the  $F(z)$  maximum varied from measurement to measurement (see Fig. 4). The maximum of  $F(z)$ , however, always coincides with the position of the minimum of the respective  $\ln[R(z)]$  function (see Fig. 4c). This circumstance enabled us to derive some generalized shape of the  $F(z)$  factor that was then applied to correct all three temperature profiles acquired with the lidar. We made use of the normalized height  $\tilde{z} = z/z_{\text{max}}$ , where  $z_{\text{max}}$  is the height at which function  $F(z)$  reaches its maximum (see Fig. 4). Then the resultant  $F(\tilde{z})$  profiles were smoothed by the use of three-point averages at normalized heights below 1.4, whereas above this level the profiles were fitted to an exponential function. The profiles of  $F(\tilde{z})$  obtained in this way are shown in Fig. 5. The average of the three shapes yielded the mean  $F(\tilde{z})$  curve (thick dashed curve) and the corresponding standard deviation  $\Delta F(\tilde{z})$ , represented in the figure by error bars. To correct the individual temperature profiles with the help of this generalized  $F(\tilde{z})$  factor we first determined

$z_{\text{max}}$  at the minimum of the  $\ln[R(z)]$  function. We then rescaled  $F(\tilde{z})$  and  $\Delta F(\tilde{z})$  and obtained  $F(z)$  and  $\Delta F(z)$  profiles, using the ratio  $z = \tilde{z} \times z_{\text{max}}$ . Several methods of near-zone temperature correction were tested. For example, in one approach we explicitly considered the decrease of the maximum of the temperature bias with increasing height (see Fig. 4b). However, none of these approaches significantly improved the results shown below.

The constants  $A_T$  and  $B_T$  in relations (8) and (9) are determined by fitting of the  $n$  measured values of  $\ln[R(n)]$  to a nonlinear function:

$$y = \ln[R_{\text{Fit}}(T_{\text{Sonde}})] = \frac{A_T}{T_{\text{Sonde}}} + B_T. \quad (19)$$

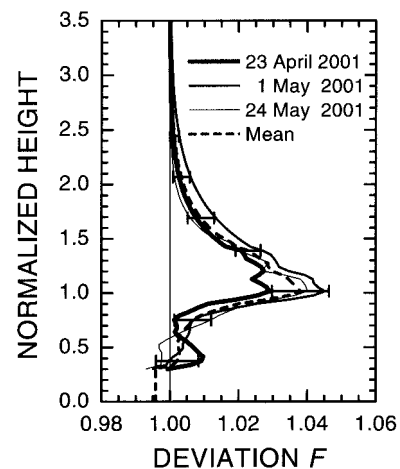


Fig. 5. Deviation  $F$  versus normalized height  $\tilde{z}$  after signal smoothing below  $\tilde{z} = 1.4$  and after the measured deviation profile is replaced by exponential fits for  $\tilde{z} \geq 1.4$ . The thick dotted curve shows the resultant mean profile of  $F$ ; errors bars indicate the standard deviation  $\Delta F$ .

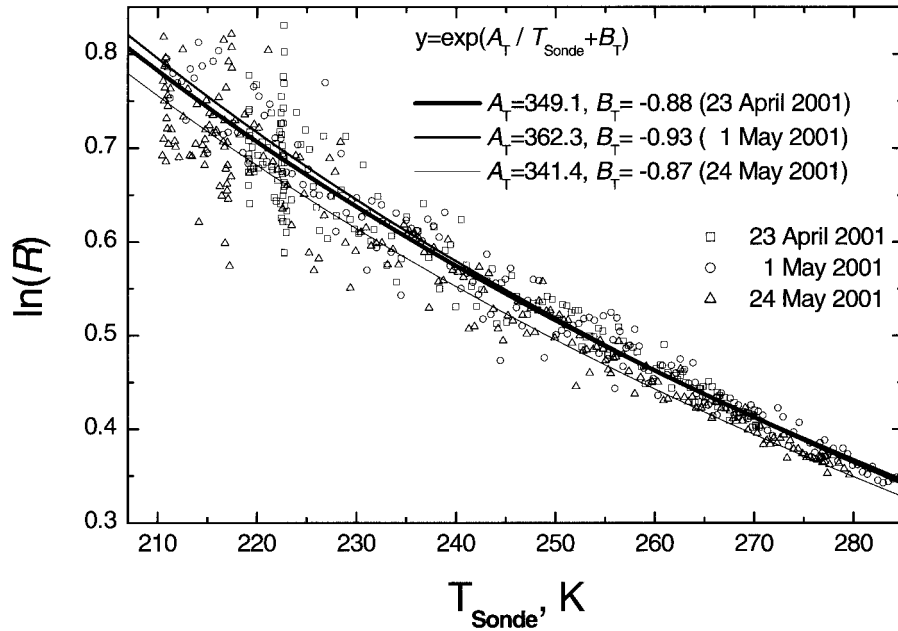


Fig. 6. Logarithm of the ratio of the rotational Raman signals  $\ln(R)$  versus radiosonde temperature  $T_{\text{Sonde}}$ . Data are fitted to  $\ln[R_{\text{Fit}}(T_{\text{Sonde}})]$ . The fits and the parameters  $A_T$  and  $B_T$  of three individual experiments are presented.

$T_{\text{Sonde}}$  is the temperature measured with the radiosonde. The Levenberg–Marquardt method is used to iteratively optimize the constants  $\Delta T_{A_T}$  and  $\Delta T_{B_T}$  such that

$$\chi^2 = \sum_{n=1}^N \frac{[\ln[R(n)] - \ln[R_{\text{Fit}}(n)]]^2}{w(n)^2} \quad (20)$$

is minimized. The statistical weights are defined as

$$w(n) = \left[ \frac{1}{P_{J_1}(z)} + \frac{1}{P_{J_2}(z)} \right]^{1/2}. \quad (21)$$

Figure 6 presents the best-fit curves for three independent radiosonde and lidar measurements performed in April and May of 2001. For the fit we used lidar data only from heights above 1700 m to minimize the distorting effect of the  $F(z)$  factor. We additionally eliminated those data with statistical errors greater than 10%. The differences in  $A_T$  and  $B_T$  determined from the three radiosonde–lidar intercomparisons arise from realignments between successive measurements.

An estimate of the standard error caused by the uncertainty in the calibration is obtained from the 95% confidence interval of  $\ln[R_{\text{Fit}}(T_{\text{Sonde}})]$ . According to this interval, the standard deviation of the temperature is 0.5–0.8 K. The basic statistical assumption in this estimation is that the lidar system parameters did not change from one experiment to another. Because such was not the case, we chose an alternative approach to estimate the temperature uncertainty. We used the three independent lidar–radiosonde measurements and calculated for each of the  $A_T$ – $B_T$  data pairs in Fig. 6 the respective temperature profile for a given measurement case. From

the resultant three temperature profiles the standard deviation  $\Delta T_{A_T, B_T}$  in Eq. (18) was found to be 2–2.5 K.

It is quite clear that in the final analysis only a larger number of radiosonde–lidar intercomparisons would provide for a more reliable calibration of the temperature channel, whereas in this study we had only three concurrent radiosonde and lidar measurements. The relative-humidity profiles presented below were calculated from lidar data and the mean values (i.e., over the three intercomparisons) of  $A_T$  and  $B_T$  as well as the mean correction factor  $F(z)$ .

Figures 7–9 present the profiles of water-vapor mixing ratios (Figs. 7a, 8a, and 9a) and temperature (Figs. 7b, 8b, and 9b) obtained with radiosondes and from lidar, as well as the profiles of relative humidity (Figs. 7d, 8d, and 9d) calculated from lidar data and measured with radiosondes on 23 April, 1 May, and 24 May 2001, respectively. Figures 7c, 8c, and 9c show the profiles of the total uncertainty in the relative humidity retrieved from lidar data as well as the error components that are due to the uncertainties in the mixing ratio and in the temperature determination. In all three cases the same data for  $F(\bar{z})$ , mean values of  $A_T$  and  $B_T$  and water-vapor calibration constant  $C^{\text{H}_2\text{O}}$  were taken, except for  $C^{\text{H}_2\text{O}}$  on 1 May 2001. On that day, a different set of neutral-density filters was used in the 387-nm nitrogen channel to protect the PMT against overload by backscattering from the near zone of the sounding path. The horizontal bars on the lidar-data curves show the confidence intervals that incorporate all the uncertainties that are inherent in these lidar measurements, as has been discussed above.

The relative humidity and the corresponding mixing ratio measured with radiosonde on 24 May 2001 are not trustworthy. A proper calibration of the

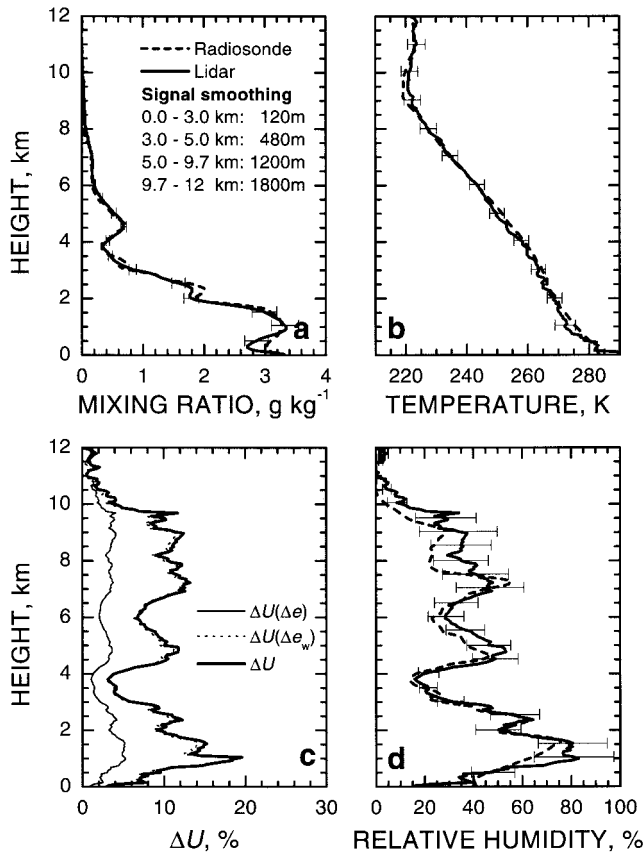


Fig. 7. a, Mixing ratio; b, temperature; c, standard deviation of the relative humidity; and d, relative humidity observed with Raman lidar on 23 April 2001, 1930–2132 UTC. All signal profiles were smoothed with the indicated window lengths before we calculated the mixing ratio and temperature. Radiosonde data were smoothed with the same window lengths. The error contributions to the total standard deviation ( $\Delta U$ ) of the relative humidity that resulted from uncertainty in the mixing ratio [ $\Delta U(\Delta e)$ ] and in the temperature [ $\Delta U(\Delta e_w)$ ] are shown in c as well.

sonde before launch was not possible. The humicap sensor of the Vaisala sondes (RS80) showed 9% in the calibration chamber with 0% relative humidity. The ground-check software accepted a resetting of the calibration value only to 5%. Thus the sonde values are all questionable. However, the temperature profile is trustworthy.

As one can see from Figs. 7c, 8c, and 9c, the strongest contribution to the total uncertainty in the relative-humidity profile comes from the error  $\Delta U(\Delta e_w)$ , which is due to the uncertainty in the lidar temperature measurements [see Eq. (15)]. It is also seen from these figures that the relative-humidity profiles of the atmosphere were determined from lidar data that were accurate to 5–20%, with the largest uncertainty at heights below  $\sim 2000$  m. That high uncertainty at low altitudes is caused primarily by the instrumental imperfection noted in the Raman-lidar temperature channel that required a correction of the temperature profiles in the near zone.

Finally, it should be stressed that the aim of this

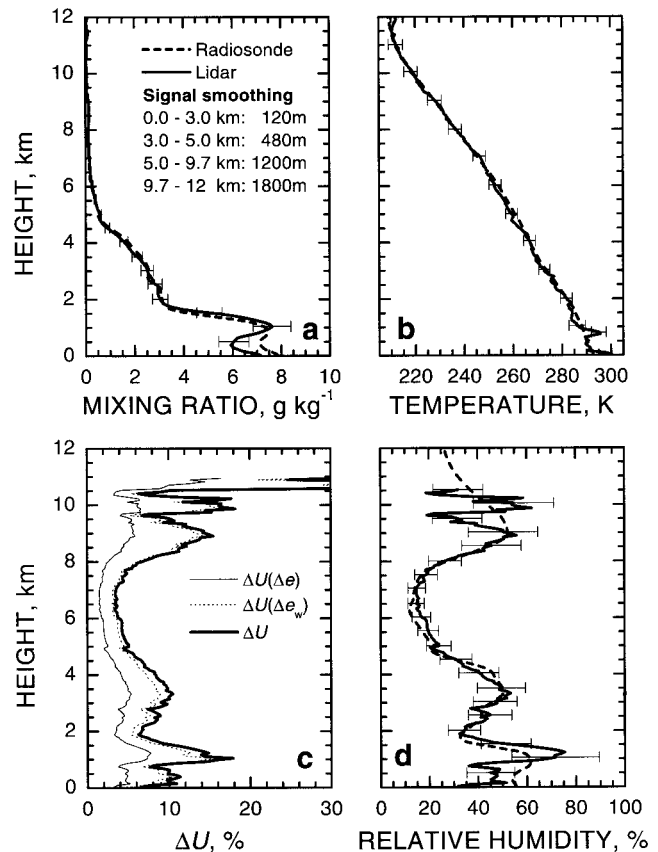


Fig. 8. Same as Fig. 7 but for observation on May 1 2001, 1919–2103 UTC.

study was to demonstrate the potential of a Raman lidar to vertically profile the relative humidity up to the tropopause. Clearly, the 2-h mean profiles shown do not meet the requirements of boundary-layer process studies as mentioned in Section 1. The limiting factor is the temperature channel. However, spatial and temporal resolution of approximately 100–200 m and 30–60 min, respectively, is achievable at daytime with the present system in the lower troposphere (below 3-km height) in combination with a sufficiently low statistical error of the relative humidity of  $\sim 10\%$  (disregarding the near-zone problem), if we assume the specifications reported in Ref. 20 for optimized Raman lidars. In this case the mixing ratio can be determined with a precision of 2% (nighttime, below 6-km height) and 7% (daytime, below 3.5-km height) and with an accuracy of  $\sim 5\%$ .

A significant increase in the temporal resolution of the temperature measurement is possible if better PMTs with higher quantum efficiency are used in the temperature channel and a second telescope is implemented for near-range observations in the lower troposphere. We recently replaced the PMTs (Thorn EMI 9893/350B; 7% quantum efficiency at 532 nm) with new ones (Hamamatsu H7421-40; 43% quantum efficiency). In addition to the signal increase by approximately a factor of 6, the use of a near-range

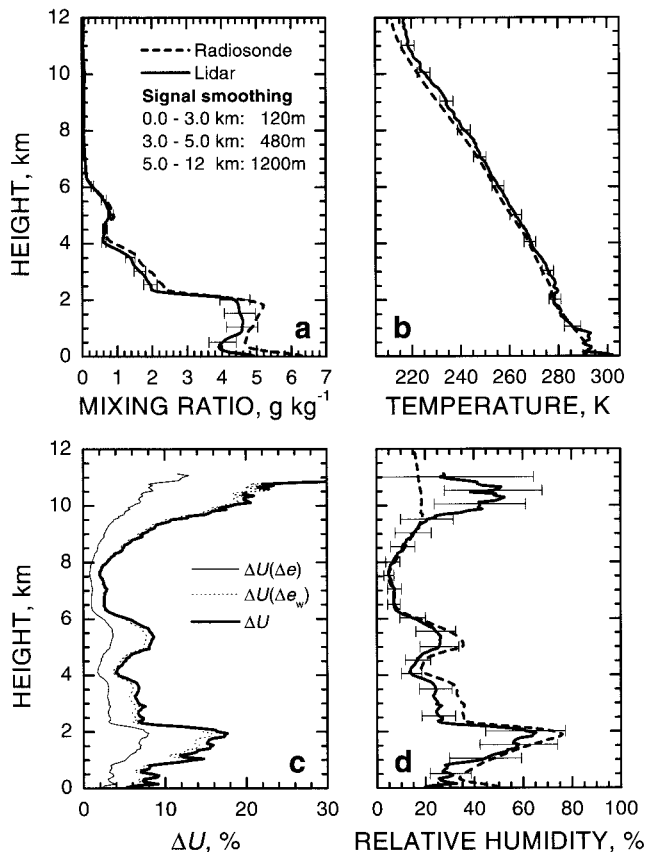


Fig. 9. Same as Fig. 7 but for observation on 24 May 2001, 2003–2158 UTC.

telescope will lead to a further increase of the signals below 1000 m by roughly a factor of 5, as model calculations show. The 1-m telescope used in this study is best for free-tropospheric and stratospheric monitoring. An increase in signal strength by a factor of 30 corresponds to an increase in the temporal resolution by approximately a factor of 5–6, so observations with a time resolution of 5–10 min should be possible with the Raman lidar after these improvements in the lower troposphere.

## 5. Conclusion

For the first time to our knowledge the water-vapor-Raman-lidar and the temperature-Raman-lidar techniques have been combined to yield the vertical profile of relative humidity throughout the troposphere. An extensive error analysis has been presented. The relative uncertainties in mixing ratio, temperature, and relative humidity are of the order of 5–10%, 1–2% (2–4 K), and 5–25%, respectively, for the Raman lidar that was used. The uncertainty in the lidar-derived temperatures dominates the error in the relative humidity. A 1–2-K accuracy is required for reducing the relative uncertainty in the relative humidity to, on average, less than 10%.

The results obtained show that this approach to profiling of relative humidity promises to yield excellent results if we take into account that this lidar is

still under development and thus its optimal capabilities have yet to be determined. The present system must be improved in terms of measurement performance in the near field. With a well-aligned and well-calibrated Raman lidar, relative-humidity profiling with 5–10-min (below 3-km height, daytime) and 1-h (free troposphere, nighttime) resolution, vertical resolution of 100 m in the boundary layer, and 500–1000 m resolution in the free troposphere in combination with a relative error of ~10% seems to be a realistic objective.

## References

1. U. Leiterer, H. Dier, and T. Naebert, "Improvements in radiosonde humidity profiles using RS80/RS90 radiosondes of Vaisala," *Contrib. Atmos. Phys.* **70**, 319–336 (1997).
2. D. Nagel, U. Leiterer, H. Dier, A. Kats, J. Reichardt, and A. Behrendt, "High accuracy humidity measurements using the standardized frequency method with a research upper-air sounding system," *Meteorol. Z.* **10**, 395–405 (2001).
3. L. M. Miloshevich, H. Vömel, A. Paukkunen, A. J. Heymsfield, and S. J. Oltmans, "Characterization and correction of relative humidity measurements from Vaisala RS80-A radiosondes at cold temperatures," *J. Atmos. Ocean. Technol.* **18**, 135–156 (2001).
4. D. M. A. Engelbart, "The use of profiling instrumentation for boundary-layer observations," in *Proceedings of the 5th International Symposium on Tropospheric Profiling: Needs and Technology*, P. T. May, ed. (Australian Bureau of Meteorology Research Centre, Adelaide, Australia, 2000), pp. 365–367.
5. A. Ansmann, M. Riebesell, and C. Weitkamp, "Measurement of atmospheric aerosol extinction profiles with a Raman lidar," *Opt. Lett.* **15**, 746–748 (1990).
6. U. Wandinger, A. Ansmann, J. Reichardt, and T. Deshler, "Determination of stratospheric-aerosol microphysical properties from independent extinction and backscattering measurements with a Raman lidar," *Appl. Opt.* **34**, 8315–8329 (1995).
7. A. Ansmann, I. Mattis, U. Wandinger, F. Wagner, J. Reichardt, and T. Deshler, "Evolution of the Pinatubo aerosol: Raman lidar observations of particle optical depth, effective radius, mass, and surface area over central Europe at 53.4° N," *J. Atmos. Sci.* **54**, 2630–2641 (1997).
8. R. A. Ferrare, S. H. Melfi, D. N. Whiteman, K. D. Evans, and R. Leifer, "Raman lidar measurements of aerosol extinction and backscattering. 1. Methods and comparisons," *J. Geophys. Res.* **103**, 19,663–19,672 (1998).
9. R. A. Ferrare, S. H. Melfi, D. N. Whiteman, K. D. Evans, M. Poellot, and Y. J. Kaufman, "Raman lidar measurements of aerosol extinction and backscattering. 2. Derivation of aerosol real refractive index, single scattering albedo, and humidification factor using Raman lidar and aircraft size distribution measurements," *J. Geophys. Res.* **103**, 19,673–19,690 (1998).
10. D. Müller, U. Wandinger, and A. Ansmann, "Microphysical particle parameters from extinction and backscatter lidar data by inversion with regularization: theory," *Appl. Opt.* **38**, 2346–2357 (1999).
11. A. Ansmann, D. Althausen, U. Wandinger, K. Franke, D. Müller, F. Wagner, and J. Heintzenberg, "Vertical profiling of the Indian aerosol plume with six-wavelength lidar during INDOEX: a first case study," *Geophys. Res. Lett.* **27**, 963–966 (2000).
12. D. Müller, F. Wagner, D. Althausen, U. Wandinger, and A. Ansmann, "Physical properties of the Indian aerosol plume derived from six-wavelength lidar observations on 25 March 1999 of the Indian Ocean Experiment," *Geophys. Res. Lett.* **27**, 1403–1406 (2000).

13. K. Franke, A. Ansmann, D. Müller, D. Althausen, and F. Wagner, "One-year observations of particle lidar ratio over the tropical Indian Ocean with Raman lidar," *Geophys. Res. Lett.* **28**, 4559–4562 (2001).
14. I. Mattis, A. Ansmann, D. Müller, U. Wandinger, and D. Althausen, "Dual-wavelength Raman lidar observations of the extinction-to-backscatter ratio of Saharan dust," *Geophys. Res. Lett.* **29**, 10.1029/2002GL014721 (2002).
15. D. D. Turner, R. A. Ferrare, L. A. Heilman Brasseur, W. F. Feltz, and T. P. Tooman, "Automated retrievals of water vapor and aerosol profiles from an operational Raman lidar," *J. Atmos. Ocean. Technol.* **19**, 37–50 (2002).
16. G. Hänel, "An attempt to interpret the humidity dependencies of the aerosol extinction and scattering coefficients," *Atmos. Environ.* **15**, 403–406 (1976).
17. V. Wulfmeyer and J. Bösenberg, "Ground-based differential absorption lidar for water vapor profiling: assessment of accuracy, resolution, and meteorological applications," *Appl. Opt.* **37**, 3825–3844 (1998).
18. E. V. Browell, S. Ismail, and W. B. Grant, "Differential absorption lidar (DIAL) measurements from air and space," *Appl. Phys. B* **67**, 399–410 (1998).
19. J. E. M. Goldsmith, F. H. Blair, S. E. Bisson, and D. D. Turner, "Turn-key Raman lidar for profiling atmospheric water vapor, clouds, and aerosols," *Appl. Opt.* **37**, 4979–4990 (1998).
20. T. M. Weckwerth, V. Wulfmeyer, R. M. Wakimoto, R. M. Hardisty, J. W. Wilson, and R. M. Banta, "NCAR–NOAA lower-tropospheric water vapor workshop," *Bull. Am. Meteorol. Soc.* **80**, 2339–2357 (1999).
21. V. Sherlock, A. Garnier, A. Hauchecorne, and P. Keckhut, "Implementation and validation of a Raman lidar measurement of middle and upper tropospheric water vapor," *Appl. Opt.* **38**, 5838–5850 (1999).
22. V. Sherlock, A. Hauchecorne, and J. Lenoble, "Methodology for the independent calibration of Raman backscatter water-vapor lidar systems," *Appl. Opt.* **38**, 5816–5837 (1999).
23. G. Poberaj, A. Assion, A. Fix, C. Kiemle, M. Wirth, and G. Ehret, "Airborne all-solid-state DIAL for water vapor measurements in the tropopause region," in *Advances in Laser Remote Sensing*, A. Dabais, C. Loth, and J. Pelon, eds. (Ecole Polytechnique, Palaiseau, France, 2001), pp. 325–328.
24. D. D. Turner, R. A. Ferrare, L. A. Heilman, and T. P. Tooman, "A two-year climatology of water vapor and aerosols in the lower troposphere measured by a Raman lidar," in *Advances in Laser Remote Sensing*, A. Dabais, C. Loth, and J. Pelon, eds., (Ecole Polytechnique, Palaiseau, France, 2001), pp. 309–312.
25. D. Bruneau, P. Quaglia, C. Flamant, and J. Pelon, "Airborne lidar LEANDRE II for water-vapor profiling in the troposphere. II. First results," *Appl. Opt.* **40**, 3462–3475 (2001).
26. C. L. Korb and C. Y. Weng, "A theoretical study of a two-wavelength lidar technique for the measurement of atmospheric temperature profiles," *J. Appl. Meteorol.* **21**, 1346–1355 (1982).
27. F. A. Theopold and J. Bösenberg, "Differential absorption lidar measurement of atmospheric temperature profiles: theory and experiment," *J. Atmos. Ocean. Technol.* **10**, 165–179 (1993).
28. J. Cooney, "Measurement of atmospheric temperature profiles by Raman backscatter," *J. Appl. Meteorol.* **11**, 108–112 (1972).
29. R. Gill, K. Geller, J. Farina, J. Cooney, and A. Cohen, "Measurement of atmospheric temperature profiles using Raman lidar," *J. Appl. Meteorol.* **8**, 225–226 (1979).
30. Y. F. Arshinov, S. M. Bobrovnikov, V. E. Zuev, and V. M. Mitev, "Atmospheric temperature measurements using a pure rotational Raman lidar," *Appl. Opt.* **22**, 2984–2990 (1983).
31. G. Vaughan, D. P. Wareing, S. J. Pepler, L. Thomas, and V. M. Mitev, "Atmospheric temperature measurements made by rotational Raman scattering," *Appl. Opt.* **32**, 2758–2764 (1993).
32. D. Nedeljkovic, A. Hauchecorne, and M. L. Chanin, "Rotational Raman lidar to measure the atmospheric temperature from ground to 30 km," *IEEE Trans. Geosci. Remote Sens.* **31**, 90–101 (1993).
33. U. Wandinger, I. Mattis, A. Ansmann, Y. F. Arshinov, S. M. Bobrovnikov, and I. Serikov, "Tropospheric temperature profiling based on detection of Stokes and anti-Stokes rotational Raman lines at 532 nm," in *Proceedings of the 19th International Laser Radar Conference*, G. Schwemmer, U. N. Singh, and S. Ismail, eds., NASA Conf. Publ. 1998-207671 (1998), Part 1, pp. 297–300.
34. A. Behrendt and J. Reichardt, "Atmospheric temperature profiling in the presence of clouds with a pure rotational Raman lidar by use of an interference-filter-based polychromator," *Appl. Opt.* **39**, 1372–1378 (2000).
35. U. Gørsdorf and V. Lehmann, "Enhanced accuracy of RASS-measured temperatures due to an improved range correction," *J. Atmos. Oceanic Technol.* **17**, 406–416 (2000).
36. G. Peters, "RASS, present state, prospects and open questions," in *Proceedings of the 5th International Symposium on Tropospheric Profiling: Needs and Technology*, P. T. May, ed. (Australian Bureau of Meteorology Research Centre, Adelaide, Australia, 2000), pp. 231–233.
37. W. F. Feltz, W. L. Smith, R. O. Knuteson, H. E. Revercomb, H. M. Woolf, and H. Ben Howell, "Meteorological applications of temperature and water vapor retrievals from the ground-based Atmospheric Emitted Radiance Interferometer (AERI)," *J. Appl. Meteorol.* **37**, 857–875 (1998).
38. D. D. Turner, W. F. Feltz, and R. A. Ferrare, "Continuous water vapor profiles from operational ground-based active and passive remote sensors," *Bull. Am. Meteorol. Soc.* **81**, 1301–1317 (2000).
39. Y. Arshinov, S. Bobrovnikov, I. Serikov, A. Ansmann, D. Althausen, I. Mattis, and U. Wandinger, "Spectrally absolute instrumental approach to isolate pure rotational Raman lidar returns from nitrogen molecules of the atmosphere," in *Advances in Laser Remote Sensing*, A. Dabais, C. Loth, and J. Pelon, eds. (Ecole Polytechnique, Palaiseau, France, 2001), pp. 121–124.
40. A. Behrendt, T. Nakamura, Y. Sawai, M. Onishi, and T. Tsuda, "Rotational vibrational–rotational Raman lidar: design and performance of the RASC Raman lidar at Shigaraki (38.8 °N, 136.1 °E), Japan," in *Lidar Remote Sensing for Industry and Environment Monitoring II*, U. N. Singh, ed., Proc. SPIE **4484**, 151–162 (2002).
41. S. M. Bobrovnikov, Y. F. Arshinov, I. B. Serikov, D. Althausen, A. Ansmann, I. Mattis, and U. Wandinger, "Daytime temperature profiling in the troposphere with a pure rotational Raman lidar," in *Lidar Remote Sensing in Atmospheric and Earth Sciences*, L. R. Bissonnette, G. Roy, and G. Vallee, eds. (Defense Research and Development Canada—Valcartier, Quebec, Canada, 2002), pp. 717–720.
42. D. D. Turner and J. E. M. Goldsmith, "Twenty-four-hour Raman lidar measurements during the Atmospheric Radiation Measurement program's 1996 and 1997 water vapor intensive observation periods," *J. Atmos. Ocean. Technol.* **16**, 1062–1076 (1999).
43. I. Mattis, U. Wandinger, D. Müller, A. Ansmann, and D. Althausen, "Routine dual-wavelength Raman lidar observations at Leipzig as part of an aerosol lidar network in Germany," in *Proceedings of the 19th International Laser Radar Conference*, G. Schwemmer, U. N. Singh, and S. Ismail, eds., NASA Conf. Publ. 1998-207671 (1998), Part 1, pp. 29–32.
44. I. Mattis, V. Jaenisch, D. Müller, K. Franke, and A. Ansmann, "Classification of particle extinction profiles derived within the framework of the German aerosol lidar network by the use of cluster analysis of backtrajectories," in *Advances in Laser Re-*

- Remote Sensing*, A. Dabais, C. Loth, and J. Pelon, eds. (Ecole Polytechnique, Palaiseau, France, 2001), pp. 211–214.
45. J. Bösenberg, M. Alpers, D. Althausen, A. Ansmann, C. Böckmann, R. Eixmann, A. Franke, V. Freudenthaler, H. Giehl, H. Jäger, S. Kreipl, H. Linné, V. Matthias, I. Mattis, D. Müller, J. Sarközi, L. Schneidenbach, J. Schneider, T. Trickl, E. Vorobieva, U. Wandinger, and M. Wiegner, “The German aerosol lidar network: methodology, data, analysis,” Rep. 317 (Max-Planck-Institut für Meteorologie, Hamburg, Germany, 2001).
  46. J. Bösenberg, A. Ansmann, J. M. Baldasano, D. Balis, C. Böckmann, B. Calpini, A. Chaikovskiy, P. Flamant, A. Hågård, V. Mitev, A. Papayannis, J. Pelon, D. Resendes, J. Schneider, N. Spinelli, T. Trickl, G. Vaughan, G. Visconti, and M. Wiegner, “EARLINET: A European Aerosol Research Lidar Network,” in *Advances in Laser Remote Sensing*, A. Dabais, C. Loth, and J. Pelon, eds. (Ecole Polytechnique, Palaiseau, France, 2001), pp. 155–158.
  47. A. Ansmann, M. Riebesell, U. Wandinger, C. Weitkamp, E. Voss, W. Lahmann, and W. Michaelis, “Combined Raman elastic-backscatter lidar for vertical profiling of moisture, aerosol extinction, backscatter, and lidar ratio,” *Appl. Phys. B* **55**, 18–28 (1992).
  48. A. Ansmann, Y. Arshinov, S. Bobrovnikov, I. Mattis, I. Serikov, and U. Wandinger, “Double-grating monochromator for a pure rotational Raman lidar,” in *Fifth International Symposium on Atmospheric and Ocean Optics*, V. E. Zuev and G. G. Matvienko, eds., Proc. SPIE **3583**, 491–497 (1998).
  49. Y. F. Arshinov and S. M. Bobrovnikov, “Use of a Fabry–Perot interferometer to isolate pure rotational Raman spectra of diatomic molecules,” *Appl. Opt.* **38**, 4635–4638 (1999).
  50. J. Zeyn, W. Lahmann, and C. Weitkamp, “Remote daytime measurements of tropospheric temperature profiles with a rotational Raman lidar,” *Opt. Lett.* **21**, 1301–1303 (1996).
  51. S. H. Melfi, J. D. Lawrence, and M. P. McCormick, “Observation of Raman scattering by water vapor in the atmosphere,” *Appl. Phys. Lett.* **12**, 40–42 (1969).
  52. J. A. Cooney, “Remote measurement of atmospheric water vapor profiles using the Raman component of laser backscatter,” *J. Appl. Meteorol.* **9**, 182–184 (1970).
  53. R. Strauch, V. Derr, and R. Cupp, “Atmospheric water vapor measurement by Raman lidar,” *Remote Sens. Environ.* **2**, 101–108 (1972).
  54. J. C. Pourny, D. Renaut, and A. Orszag, “Raman-lidar humidity sounding of the observation of Raman scattering by water vapor in the atmosphere,” *Appl. Opt.* **18**, 1141–1148 (1979).
  55. D. Renaut, J. C. Pourny, and R. Capitini, “Daytime Raman-lidar measurements of water vapor,” *Opt. Lett.* **5**, 233–235 (1980).
  56. J. A. Cooney, K. Petri, and A. Salik, “Measurements of high resolution atmospheric water-vapor profiles by use of a solar blind Raman lidar,” *Appl. Opt.* **24**, 104–108 (1985).
  57. D. Renaut and R. Capitini, “Boundary-layer water vapor probing with a solar-blind Raman lidar: validations, meteorological observations and prospect,” *J. Atmos. Ocean. Technol.* **5**, 585–601 (1988).
  58. G. Vaughan, D. P. Wareing, L. Thomas, and V. Mitev, “Humidity measurements in the free troposphere using Raman backscatter,” *Q. J. R. Meteorol. Soc.* **114**, 1471–1484 (1988).
  59. S. H. Melfi, D. N. Whiteman, and R. A. Ferrare, “Observation of atmospheric fronts using Raman lidar moisture measurements,” *J. Appl. Meteorol.* **28**, 789–806 (1989).
  60. D. N. Whiteman, S. H. Melfi, and R. A. Ferrare, “Raman lidar systems for the measurement of water vapor and aerosols in the Earth’s atmosphere,” *Appl. Opt.* **31**, 3068–3082 (1992).
  61. D. N. Whiteman, W. F. Murphy, N. W. Walsh, and K. D. Evans, “Temperature sensitivity of an atmospheric Raman lidar system based on a XeF excimer laser,” *Opt. Lett.* **18**, 247–249 (1993).
  62. A. Ansmann, M. Riebesell, U. Wandinger, C. Weitkamp, and W. Michaelis, “Tropospheric water vapor measurement by Raman lidar: atmospheric extinction correction,” in *Proceedings of the 15th International Laser Radar Conference*, V. E. Zuev, ed. (Institute of Atmospheric Optics, Tomsk, Russia, 1990), pp. 256–259.
  63. R. A. Ferrare, S. H. Melfi, D. N. Whiteman, K. D. Evans, F. J. Schmidlin, and D. Starr, “A comparison of water vapor measurements made by Raman lidar and radiosondes,” *J. Atmos. Ocean. Technol.* **12**, 1177–1195 (1995).
  64. B. A. Bodhaine, N. B. Wood, E. G. Dutton, and J. R. Slusser, “On Rayleigh optical depth calculations,” *J. Atmos. Ocean. Technol.* **16**, 1854–1861 (1999).
  65. R. R. Rogers and M. K. Yau, *A Short Course in Cloud Physics* (Pergamon, New York, 1988).
  66. R. J. List, ed., *Smithsonian Meteorological Tables* (Smithsonian Institution, Washington, D.C., 1951).
  67. I. B. Serikov, Y. F. Arshinov, S. M. Bobrovnikov, D. Althausen, and I. Mattis, “Distortion of the temperature profile of the atmosphere acquired with a pure rotational Raman lidar due to sphericity of the Fabry–Perot interferometer plates,” in *Lidar Remote Sensing in Atmospheric and Earth Sciences*, L. R. Bissonnette, G. Roy, and G. Vallee, eds. (Defense Research and Development Canada—Valcartier, Quebec, Canada, 2002), pp. 721–724.